Fabrication of CdS/titanium-oxo-cluster nanocomposites based on a Ti_{32} framework with enhanced photocatalytic activity for tetracycline hydrochloride degradation under visible light

Qi Zhu[a,b], Yukun Sun[a,b], Feisha Na[a,b], Juan Wei[a,b], Shuai Xu[a,b], Yuliang Li[a,b,*], Feng Guo[c]

[a] *School of Environmental Science and Engineering, Chang'an University, Xi'an, 710064, China*
[b] *Key Laboratory of Subsurface Hydrology and Ecological Effects in Arid Region, Ministry of Education, 710064, Xi'an, China*
[c] *School of Energy and Power Engineering, Jiangsu University of Science and Technology, Zhenjiang, Jiangsu, 212003, China*

ARTICLE INFO

ABSTRACT

In this work, CdS/Ti_{32}-oxo-cluster (CTOC) composites were first synthesized via in situ precipitation and ultrasonic methods. The experimental results demonstrated that CdS nanoparticles uniformly decorated the surface of CTOC with high specific area and microporous to form composite structures. Meanwhile, the CdS/CTOC composites exhibited an excellent high rate of photocatalytic activity for tetracycline hydrochloride (TC) degradation under visible light irradiation, and the activity performance was approximately 4.49 and 16.36-fold higher than that of pure CdS and CTOC, respectively. Moreover, The Ti^{3+} signal was detected by electron paramagnetic resonance (ESR) technique after irradiation, and the superoxide radical ($\cdot O_2^-$) and holes (h^+) were proven to be the main active species during the degradation of TC. Photocatalytic mechanism and intermediates over CdS/CTOC composites were elucidated and corresponding reaction model and degradation routes of TC were presented. It is anticipated that this work could boost new insight on CdS/ CTOC binary composite systems to effectively degrade organic pollutants, which given a strategy for application on practical industry.

1. Introduction

Tetracycline hydrochloride (TC) has been widely used in the pharmaceutical industry, animal husbandry and aquaculture to resist infection over the past few decades [1,2]. However, due to TC cannot be completely metabolized by humans and animals, a large amount of ingested TC is excreted through stools and urine into various water bodies, resulting in detrimental effects on human health and the ecosystem [3–5]. In this regard, treating TC from aqueous solutions is an urgent necessity. Methods such as adsorption [6,7], electrochemistry [8], photocatalysis [9,10] and so on have been used to remove and degrade TC. Compared with conventional methods, photocatalytic technology utilizing inexhaustible solar light and semiconductor materials [11,12] has been proven to be a green and sustainable strategy to utterly eliminate environmental pollutants. However, single-component photocatalysts often have several inherent drawbacks, such as wide bandgap, poor absorption in the visible region and rapid recombination of photogenerated electron-hole pairs; thus, it is highly desirable to design composite photocatalytic systems for high-efficiency treatment of TC.

Cadmium sulfide (CdS) with a suitable conduction band and high visible-light-induced activity has been spotlighted and extensively employed as a photocatalyst for organic pollutant degradation [13–15]. However, the main drawbacks of CdS are the rapid recombination of electron-hole pairs and few catalytic sites, which limited its further application in photocatalysis field [16,17]. To date, numerous efforts have been made to improve the photocatalytic performance of CdS, such as coupling CdS with wide bandgap nanomaterials [18,19], modifying CdS morphology [20–22], and incorporating CdS in porous materials [23–25], etc. Among these efforts, the construction of the CdS/TiO_2 coupled system has resulted in substantial research in solar photocatalysis applications due to their matched band structures and apposite optical properties. Recently, various CdS/TiO_2 nanocomposite photocatalytic materials have been used as photocatalytic degradation of organic pollutants (Table S1, supporting information). However, because the synthesis conditions of the two components do not match, an effective synthetic strategy for increasing the number of catalytic sites of CdS by incorporating large surface area materials has not been applied to CdS/TiO_2 composites. Therefore, the above composite systems exhibit an unsatisfactory degradation efficiency of organic

* Corresponding author at: School of Environmental Science and Engineering, Chang'an University, Xi'an, 710064, China.
E-mail addresses: 782612986@qq.com (Q. Zhu), yulianglee@hotmail.com (Y. Li).

pollutants and it still remains an urgent need to construct an efficient CdS-based organic degradation system.

Titanium oxo-clusters (TOCs) have received tremendous attention in recent years due to the photocatalytic properties similar to TiO_2 and their precise atomic structure [26–28]. During the past decade, TOCs with various structure types and its derivatives have been reported [29–33], but there have been relatively few systematic studies on modifications of their bandgap and photocatalytic activity. Recently, a cyclic Ti_{32}-oxo-cluster (CTOC) with a high specific surface and microporous surface was reported [34]. As the TOC with the largest specific surface area ($^-500\ cm^2\ g^{-1}$) reported so far, the Ti_{32}-oxo-cluster possesses permanent micropore and eight connected Ti_4 tetrahedral cage units, which can provide more reaction sites and adsorb more organic molecules during a photocatalysis process. Meanwhile, the existence of carboxyl ligands on the surface allows Ti_{32}-oxo-cluster to be tightly connected into an ordered array of bulk structure. Despite these considerable advantages, the main drawbacks of a single TOC (*e.g.,* wide bandgap, poor light absorption and rapid charge recombination, etc.) have greatly impeded large-scale applications in solar-driven degradation of organic pollutants. Therefore, it is extremely important to develop visible-light-responsive TOC-based catalysts.

According to the aforementioned motivation and considering the complementary optical and photocatalytic properties of the Ti_{32}-oxo-cluster and CdS, for the first time, we attempt to incorporate CdS with the Ti_{32}-oxo-cluster to form efficient visible-light-driven organic degradation catalysts with many unique advantages in contrast with CdS/ TiO_2: i) As the precursor of TiO_2, the Ti_{32}-oxo-cluster has a suitable energy band structure and high specific surface area; incorporating CdS in the Ti_{32}-oxo-cluster can increase the number of catalytic sites and improve the separation efficiency of photogenerated charges of CdS. ii) The bandgap and light absorption performance of the Ti_{32}-oxo-cluster can be effectively modified by intimate interface contact with CdS. iii) due to the surface are modified by doubledeprotonated ethylene glycolates [35], the Ti_{32}-oxo-cluster can create an effective composite synthesis condition through rich intermolecular interactions.

Herein, we designed and constructed a small quantity of CdS (0.3–5 wt.%) on the surface of the Ti_{32}-oxo-cluster by in situ precipitation and ultrasonic methods to form a composite structure. The CdS/Ti_{32}-oxo-cluster composites exhibited excellent degradation rate of TC under visible-light irradiation, far exceeding that of the pure CTOC and CdS, and an optimal content of CdS was also determined. On the basis of these results, a cycling experiment was also carried out to detect the stability of the photocatalyst. Additionally, a detailed mechanism for the degradation of TC over the CdS/Ti_{32}-oxo-cluster composite photocatalysts is proposed.

2. Experimental section

2.1. Preparation of the photocatalysts

2.1.1. Preparation of Ti_{32}-oxo-cluster

All reagents for the synthesis and analysis were commercially available and used without further treatment. The Ti_{32}-oxo-cluster was synthesized through a typical facile solvothermal method in a closed glass container [34]. Pivalic acid (1.07 g, 10.51 mmol) and tetrabutyl titanate (1.7 ml, 4.98 mmol) were mixed in 20 ml ethylene glycol and heated at 100 °C for 24 h to form a white precipitate. The obtained products were washed with tetrahydrofuran three times and dried under vacuum.

2.1.2. Synthesis of CdS

CdS was prepared by the direct precipitation method. Briefly, $CdCl_2·2.5H_2O$ (0.77 g, 3.39 mmol) and $Na_2S·9H_2O$ (0.68 g, 2.84 mmol) were added to two beakers containing 10 ml anhydrous ethanol and 5 ml deionized water, respectively. After stirring for 30 min, Na_2S was added to the $CdCl_2$ solution with continuous magnetic stirring, and the

mixture was transformed into an orange floccus. After washing the precipitate with distilled water and anhydrous ethanol several times, the powder was dried at 80 °C overnight.

2.1.3. Synthesis of the CdS/Ti_{32}-oxo-cluster composites

First, 0.2 g Ti_{32}-oxo-cluster was added to a beaker containing 30 ml deionized water and sonicated for 30 min until evenly dispersed to form the white solution A. Then, $CdCl_2·2.5H_2O$ (0.0032 g, 0.014 mmol) and $Na_2S·9H_2O$ (0.0033 g, 0.014 mmol) were added to 10 ml anhydrous ethanol and 5 ml deionized water to form solution B and solution C, respectively. Under constant stirring conditions, solution B and solution C were added slowly into solution A and sonicated for 6 h. The procured composite was washed with distilled water three times and dried at 65 °C for 8 h. On this basis, CdS/Ti_{32}-oxo-cluster composites with different mass ratios of CdS (0.3 wt.%, 0.5 wt.%, 1 wt.%, 3 wt.% and 5 wt. %) were prepared and denoted as CT-0. 3, CT-0. 5, CT-1, CT-3 and CT-5, respectively.

2.2. Characterization methods

Powder X-ray diffraction (XRD) analysis was performed using X-ray diffraction with a 'Pert-ProMPD/max-γAX-ray (Holland) diffractometer with Cu Kα radiation (λ =0.15406 nm). Electrospray ionization mass spectrometry (ESI-MS) was obtained by Thermo Fisher Scientific LTQ XL mass spectrometer. Fourier transform-infrared spectroscopy (FT-IR) was recorded by a Nicolet 330 spectrometer with KBr as the reference sample. The Raman spectra were obtained on an HR 800 Raman spectrometer (JY, France). Scanning electron microscopy (SEM) images were obtained by a Sitatou S-4800 instrument. The surface elemental composition was detected by an energy dispersive X-ray spectrometer (EDX) attached to the SEM. Transmission electron microscopy (TEM) images of the internal morphology and grain characteristics of the catalyst were recorded by a JEM-2010 F instrument. N_2 adsorption–desorption isotherms of the catalysts were obtained on a Micromeritics ASAP 2020 gas adsorption analyzer. X-ray photoelectron spectroscopy (XPS) were analyzed by the Axis ultra-DLD X-ray photoelectron spectrometer. The UV–vis absorption spectra of the as-prepared samples were characterized by a Lambda 750 spectrophotometer in the wavelength range of 200–800 nm. Electrochemical analyses were performed on a CHI 660b workstation. The Pt wire, saturated calomel electrode and prepared sample electrode served as the counter electrode, reference electrode and working electrode, respectively. A 300 W Xe lamp xenon lamp (λ < 420 nm) and 0.5 M sodium sulfate (Na_2SO_4) were used as the light source and electrolyte, respectively.

2.3. Investigation of photoactivity

First, the initial absorbance of TC was measured by a UV–vis spectrophotometer at the maximum absorption wavelength of 357 nm. Then, 10 mg of photocatalyst was added to the TC aqueous solution (50 mL, 50 mg/L). Before visible-light irradiation, the solution was stirred in the dark for 30 min to ensure adsorption equilibrium. A 300 W xenon lamp was used as the visible-light source, and a filter was used to filter the light of λ < 420 nm. 3 mL of the suspension was removed at intervals, filtered through a 0.45 μm filter membrane and analyzed on a UV–vis spectrophotometer.

The intermediates produced in the photodegradation process of TC were identified by high performance liquid chromatography-mass spectrometry (Agilent, 6460 Triple Quad LC/MS series). Mobile phase was a mixture of acetonitrile and formic acid (0.1%) with a flow rate of 0.25 mL/min. The injection volume was 5.0 μL. The fragment voltage was 135 V and the capillary voltage was 2800 V. The mass range of the MS is m /z 200-500.
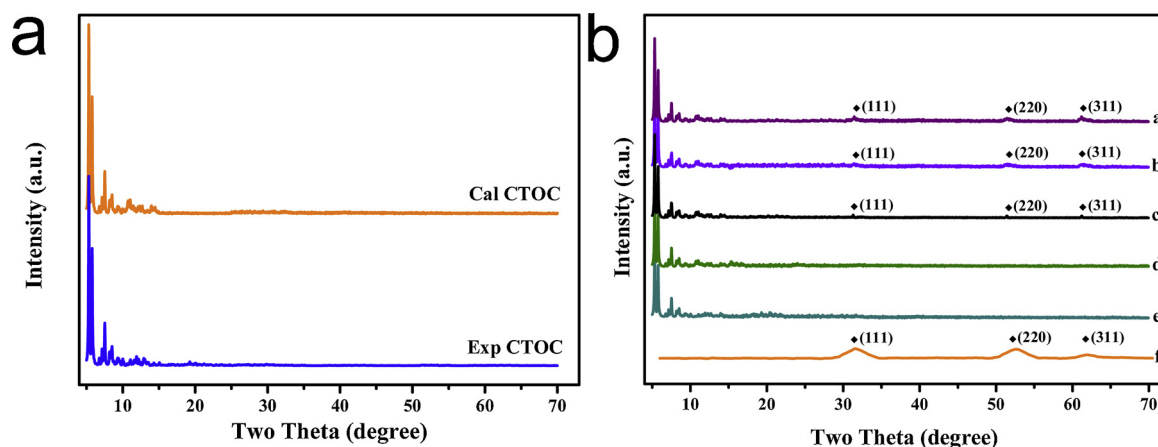
Fig. 1. (a) XRD patterns of the calculated CTOC and experimental CTOC. (b) XRD patterns of CdS and CdS/CTOC composites: (a) CT-5, (b) CT-3, (c) CT-1, (d) CT-0.5 (e) CT-0.3 and (f) CdS.

2.4. Capture experiment

Before light irradiation, sacrificial agents, such as 0.5 mmol isopropanol (IPA), 0.5 mmol disodium edetate (EDTA-2Na) and 0.5 mmol benzoquinone (BQ), were added to the solution to probe the presence of hydroxyl radicals ($\cdot OH$), holes (h^+) and superoxide radicals ($\cdot O_2^-$), respectively. In addition, $\cdot O_2^-$ radicals and Ti^{3+} species were measured by the electronic spin resonance (ESR) technique under visible-light irradiation ($\lambda > 420$ nm).

3. Results and discussion

3.1. Characterization of the CdS/ Ti_{32}-oxo-cluster composites

The phase purity and crystal phase composition of the prepared samples were determined by XRD measurements (Fig. 1). It can be observed from the profiles that the experimentally obtained XRD data are consistent with the simulated data, proving the formation of the high-purity Ti_{32}-oxo-cluster phase. Meanwhile, the experimental results of ESI-MS of CTOC (Fig.S1) are agreement with that of XRD, which is same to the reported in the previous literature [34]. With respect to the CT-1 composite, the three additional weak peaks at $2\theta = 30.8°$, $51.4°$, and $61.2°$ can be attributed to the (111), (220), and (311) crystal planes of CdS, which is also completely match to the XRD diagram of cubic phase CdS in Fig. 1b [36]. And a group of strong diffraction peaks below 15° in the pattern of CT-1 indicated that the structure of the Ti_{32}-oxo-cluster was well retained after CdS loading. In addition, the CdS/Ti_{32}-oxo-cluster samples with different contents in Fig. 1b also presented a mixture of characteristic peaks until the decorating content increased to 1%, and the diffraction peaks of CdS gradually strengthen as the content further increased. Additionally, the characteristic peaks of the Ti_{32}-oxo-cluster did not vary in intensity or shape in all samples, demonstrating that the structure of the Ti_{32}-oxo-cluster was unchanged. In conclusion, the results indicate the coexistence of CdS and the Ti_{32}-oxo-cluster phase in the obtained composites.

To further determine the structure and interactions of the CdS/ CTOC photocatalysts, the samples were analyzed by FT-IR analysis. As shown in Fig. 2a, for the CTOC and CT-1 samples, the broad peaks at approximately 3400 cm^{-1} can be ascribed to absorbed surface hydroxyl groups (water molecular) [37]. Some characteristic absorption peaks located at 1600-1500 cm^{-1} can be attributed to the chelation of carboxylic acid groups. The ν_{C-H} (between 2926 and 2850 cm^{-1}) and ν_{Ti-O-C} (1010 and 1006 cm^{-1}) peaks are due to the vibration of ethylene glycol. The broad peak in the region centered at approximately 720 cm^{-1} corresponds to the Ti-O vibration mode. Further careful observation in Fig. 2a, it can find that the main vibrational peak of the CT-

1 is similar to that of the pure cluster and also displays an additional CdS satellite peak at 1130 cm^{-1} [38]. Raman spectroscopy is an analytical method for studying molecular structures based on molecular vibration and rotation information. The Raman spectra (Fig. 2b) of the CdS/CTOC and pure CTOC also show that in addition to the corresponding bands of CTOC, CT-1 exhibits resonant raman response peaks at approximately 300, 600, and 900 cm^{-1}, which can be attributed to the 1LO, 2LO, and 3LO longitudinal optical phonon mode bands of CdS [39], respectively. Based on the above analysis, we verified the coexistence of both CdS and CTOC and the successful formation of CdS/ CTOC binary composites, which is consistent with the XRD analysis results.

To investigate the microstructure and crystalline structure of the CdS/CTOC composites, we used scanning electron microscopy (SEM) and high-resolution transmission electron microscopy (HR-TEM) to observe the CTOC and CT-1 composites (Fig.S2-S3). As the SEM micrographs show (Fig.S2), the surface morphology of bulk CTOC became relatively rough after the combination of CdS. Significantly, well-dispersed CdS nanoparticles were uniformly deposited on the surface of the CTOC to form the intimate composite structure, and these nanoparticles can provide more photocatalytic reaction sites on the surface of the CTOC to enhance the photocatalytic activity of the composites. The TEM image of CT-1 shows the CdS particles compared to the TEM images of pure CTOC (Fig.S3), and the lattice spacing of 0.36 nm in the HRTEM image indicates the (100) crystal plane of cubic CdS; these results also further confirm the formation of CdS/CTOC composites. Meanwhile, the EDS elemental microanalysis results shown in Fig.S1 clearly indicate that in addition to Ti, O, C and H on the nanocomposite surface, Cd and S are present in the CT-1 sample in an atomic ratio of 1:1, providing further evidence of the successful preparation of composite photocatalytic materials.

XPS technique was performed to further investigate the composition and elemental valence of the samples we prepared. It can be seen from Fig. 3a that the survey spectra of CT-1 clearly discloses the characteristic peaks of C1 s, Ti2p, O1 s, Cd3d and S2p, which also indicates these elements exist in the nanocomposite. Fig. 3b shows the high-resolution spectrum of C1 s for CTOC and CT-1. The C1 s peak in CTOC can be fitted into two peaks, which reveals two C1 s states in the C−O bond (285.9 eV) [40] and the surface adsorption of carbon (284.6 eV). The fitted peaks of Ti2p and O1 s of CTOC and CT-1 are shown in Fig. 3c,d. For the Ti2p spectrum (Fig. 3c), the peaks at 459.6 eV and 464.9 eV in CTOC can be attributed to $Ti2p_{3/2}$ and $Ti2p_{1/2}$, which also proves the presence of Ti^{4+} on the surface of the CTOC [41]. The O1 s peaks observed at 532.4 eV and 530.7 eV in CTOC arise from the surface-adsorbed oxygen and lattice oxygen [42]. Compared with pure CTOC, the positive shift of C1 s, Ti2p and O1 s characteristic peaks are observed in
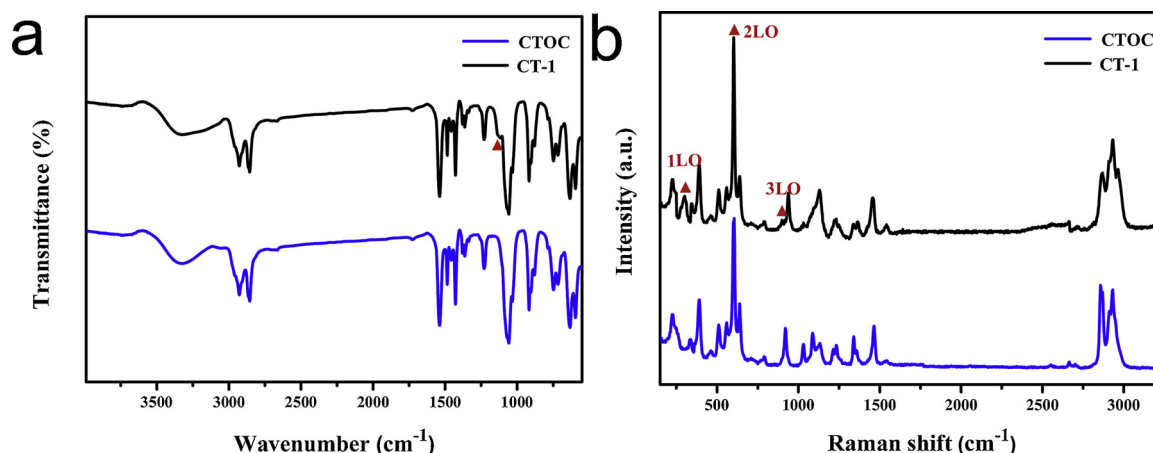
Fig. 2. (a) FT-IR and (b) Raman spectra of CTOC and CT-1.

the CT-1, indicating the chemical environment of C, Ti and O in CTOC have changed after incorporation with CdS. The same phenomenon occurs in the high-resolution XPS spectra of S2p and Cd3d (Fig. 3e-f). Compared with CdS, the S2p (160.1 eV, $2p_{3/2}$) and (161.3 eV, $2p_{1/2}$) [43], Cd3d (404.1, $3d_{3/2}$) and (411.2, $3d_{5/2}$) [44] in the CT-1 shows a shift toward lower binding energies, implying the binding energies of Cd and S have been influenced and there is a strong interaction among the CdS and CTOC. The XPS results clearly proved that the composite structure has been built between CdS and CTOC, which provide access to promote the transport and separation of electrons and holes.

The UV–vis spectroscopy measurements were conducted to determine the light absorption properties of the as-prepared samples (Fig. 4). Obviously, the pristine Ti_{32}-oxo-cluster (white powder, orange line) exhibits a significant absorption edge up to 490 nm, and the CdS (yellow powders, blue line) absorption sideband is at approximately 650 nm [36]. More importantly, after the CdS nanoparticles are uniformly deposited on the cluster, the CdS/CTOC composite (yellow powder, black line) exhibits an enhanced photoresponse in the visible region, and an absorption band is observed in the spectrum extending to 760 nm, which facilitates usage of the solar spectrum. At the same time, the bandgap energy (E_g) of the semiconductors were also estimated by the plot of $(ah\nu)^2$ versus the photon energy ($h\nu$) [45]. The E_g values of CdS, CTOC and CT-1 were calculated to be 2.07, 3.41 and 2.10 eV, respectively. The above results show that the introduction of CdS not only broadens absorption capacity in the visible region but also reduces E_g, allowing CdS/CTOC composites to be activated by visible-light irradiation, which greatly enhances their photocatalytic activity. To better investigate the energy band structure, VB-XPS and Mott-Schottky plots were performed to estimate the valence band maximum (VBM) and conduction band maximum (CBM) positions of the samples [46,47]. It can be seen from Fig. 4c that the VBM values of CdS and CTOC are 0.77 eV and 2.21 eV, respectively. Moreover, the VBM value of anatase TiO_2 was measured under the same conditions to correct and estimate the valence band of the samples we prepared [48], which is determined to be 2.23 eV (Fig.S4). According to the reported CBM of anatase TiO_2 (-0.4 eV vs. NHE) [49], the VBM value of anatase TiO_2 could be calculated to be 2.83 eV combine with its band gap (3.23 eV, Fig.S4). Consequently, the VBM positions of CdS and CTOC were corrected to 1.37 eV and 2.81 eV. The flat-band potentials reflected by Mott-Schottky plots (Fig. 4d) can be used to estimate the CBM positions of the CdS and Ti_{32}-oxo-cluster. The positive slopes reveal that the CdS and Ti_{32}-oxo-cluster are typical n-type semiconductors, and the flat-band potentials of the CdS and Ti_{32}-oxo-cluster are -1.17 and -1.07 V versus Ag/AgCl, which equals to -0.56 and -0.46 V when using a standard hydrogen electrode as a reference. It has been reported that the flat-band potential is 0.1-0.3 eV higher than the CBM potential in an n-type semiconductor [50]. Thus, the CBM potentials of CdS and Ti_{32}-oxo-

cluster were estimated to be -0.70 and -0.60 V. The determination of the band position helps to further understand the electron transfer process and the reaction mechanism of the CdS/CTOC composites photocatalyst system.

3.2. Photocatalytic activity of the CdS/Ti_{32}-oxo-cluster composites

Nitrogen adsorption-desorption isotherms of all as-prepared samples were applied and shown in Fig. 5a and Table 1. Because composite photocatalysis is a surface-dependent phenomenon, the Brunauer–-Emmett–Teller (BET) surface area and total pore volume have a great influence on the photocatalytic activity. As shown in Fig. 5a, the BET surface area of all the composites is slightly lower than that of the pure CTOC (485.1 $m^2 g^{-1}$), and the BET surface area gradually decreases as the load content of CdS further increased. The number of effective active sites has a great relationship with the specific surface area [51]. Therefore, the as-synthesized CdS/CTOC composite catalysts still have a high BET surface area and abundant photocatalytic reaction sites to adsorb organic molecules and intermediate products during a photocatalysis process. Adsorption experiments were carried out before the photocatalytic degradation of TC. It can be seen from Fig. 5b that all photocatalysts have reached the adsorption equilibrium within 30 min under dark conditions. And all materials adsorption properties are proportional to its BET surface area.

TC aqueous solution was degraded under visible light to evaluate the photocatalytic activity of the synthesized samples. In Fig. 6a, TC was not observed to have obvious degradation in the blank experiment, indicating that the contribution of TC self-photolysis could be ignored. For the pure sample of as-prepared CdS, the degradation rate was 62.6% under visible-light irradiation after 60 min. This rate can be attributed to the monomer CdS photocatalyst having a high photogenerated carrier recombination rate and few catalytic sites, resulting in its low photocatalytic activity. Although it does not respond to visible light, the Ti_{32}-oxo-cluster can slowly degrade TC under visible light, which may be due to the photosensing ability of TC [52]. As expected, when CdS decorated the surface of the Ti_{32}-oxo-cluster, the photocatalytic activity of the CdS/CTOC composites were greatly enhanced. As displayed in Fig. 6a, as the amount of CdS introduced increases, the photocatalytic performance of the CdS/CTOC composites increase. When the mass fraction of CdS loading is 1%, the photocatalytic degradation rate of the CdS/CTOC composite is the highest, reaching 96.3% within 60 min. However, further addition of more than 1 wt.% CdS results in a significant decrease in the final degradation efficiency. This phenomenon can be attributed to the fact that an appropriate amount of CdS can increase the reaction sites on the surface of the CTOC, and excessive loading of CdS nanoparticles can cause agglomeration and shadowing effects [53]. Fig. 6b shows that the
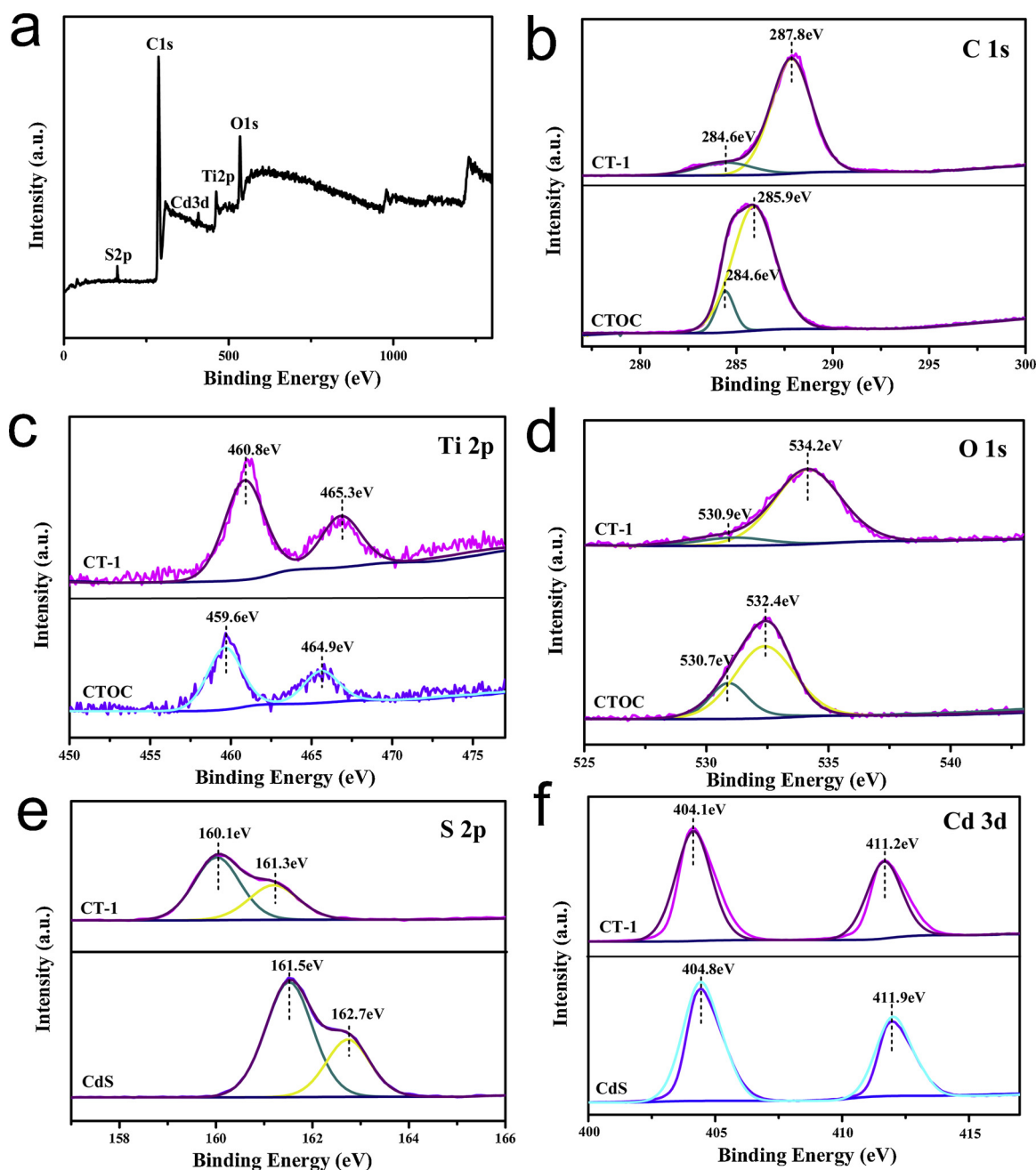
Fig. 3. XPS spectra of CdS, CTOC and CT-1 samples. (a) The survey spectra of CT-1; (b) C 1s XPS spectra; (c) Ti 2p XPS spectra; (d) O 1s XPS spectra; (e) S 2p XPS spectra; (f) Cd 3d XPS spectra.

characteristic absorption peak of TC (200–600 nm) is gradually weakened within 60 min in the presence of CT-1 as a photocatalyst. Fig. 6c shows the kinetic characteristic of the photocatalytic reaction process with the synthesized sample, and these results indicate that the photocatalytic reaction in this study conforms to the first-order reaction kinetics equation. Fig. 6d is a bar graph of the kinetic reaction rate constants of the different photocatalysts. It is clear that the 1% CdS/CTOC composite photocatalyst has the optimal activity and highest degradation rate constant, which is 4.49 and 16.36 times higher than that of the pure CdS and CTOC, respectively.

3.3. Clarification of the reaction mechanism

In order to investigate the reasons for the intensified photocatalytic activity of the CdS/CTOC composite structures, photocurrent-time

measurements and EIS were applied to characterize all as-prepared samples. As shown in Fig. 7a, the transient photoresponse current density of all the composite photocatalysts is significantly higher than that of the pure CdS and CTOC, and the light response intensity of the samples is proportional to its photocatalytic activity of TC. This result fully illustrates the existence of built-in electric field in the composite structure, which can effectively improve the mobility of photo-generated carriers between CdS and clusters [54]. Simultaneously, an EIS analysis was also performed. Fig. 7b shows that the synthesized CdS/CTOC composites has a smaller semicircle than the pure CdS and CTOC and CT-1 has the smallest arc radius, indicating that the composites have more efficient separation of electron-hole pairs. The EIS Nyquist plots also confirmed that the charge resistance of CTOC decreases after loading CdS, which indicates that the decorate of CdS can accelerate the interface charge transfer. In addition, the EIS
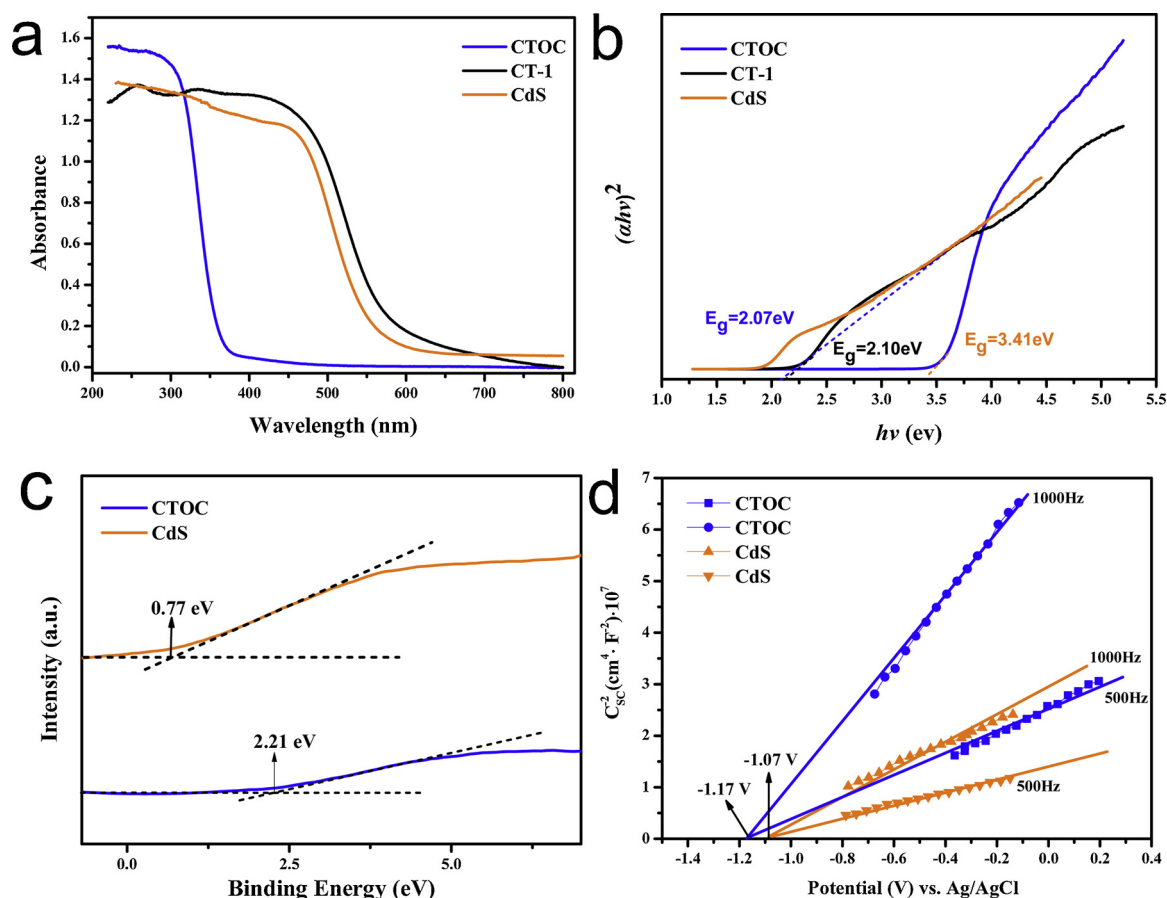
Fig. 4. (a) UV–vis absorption spectra of CdS, CTOC and the CT-1 and (b) the plots of $(\alpha h v)^2$ versus photon energy ($h v$) for the bandgap energies of CdS, CTOC and the CT-1 by Kubelka-Munk equation. (c) valence band XPS spectra and (d) Mott-Schottky plot of CdS and CTOC.
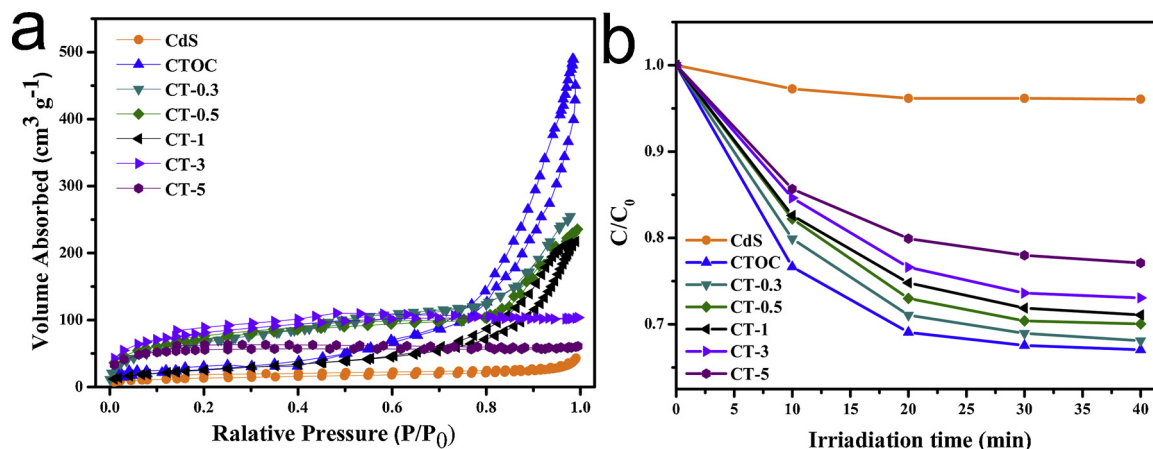
measurements of CT-1 was performed under both light and dark conditions (Fig.S5), and the results showed that CT-1 had a smaller radius under illumination, which consistent with the trend of the electronic conductivity of the electrode.

In this study, capture experiments were used to ascertain the photocatalytic mechanism of the composites. Three capture agents, IPA (capture ·OH), EDTA-2Na (capture h^+) and BQ (capture ·O_2^-), were used to determine the main active species in the photocatalytic process. Fig. 8c shows that the photocatalytic degradation rate of TC was reduced from 96.4% to 14.7% and 20% after BQ and EDTA-2Na were added to the above solution respectively, illustrating that ·O_2^- and

Table 1
Pore characteristics and BET surface area of the all as-prepared samples.

sample	S_{BET} (m^2 g^{-1})	Pore Volume (cm^3 g^{-1})
CdS	94.09	0.34
CTOC	485.13	0.46
CT-0.3	382.08	0.36
CT-0.5	357.15	0.27
CT-1	365.45	0.24
CT-3	249.75	0.18
CT-5	192.67	0.09

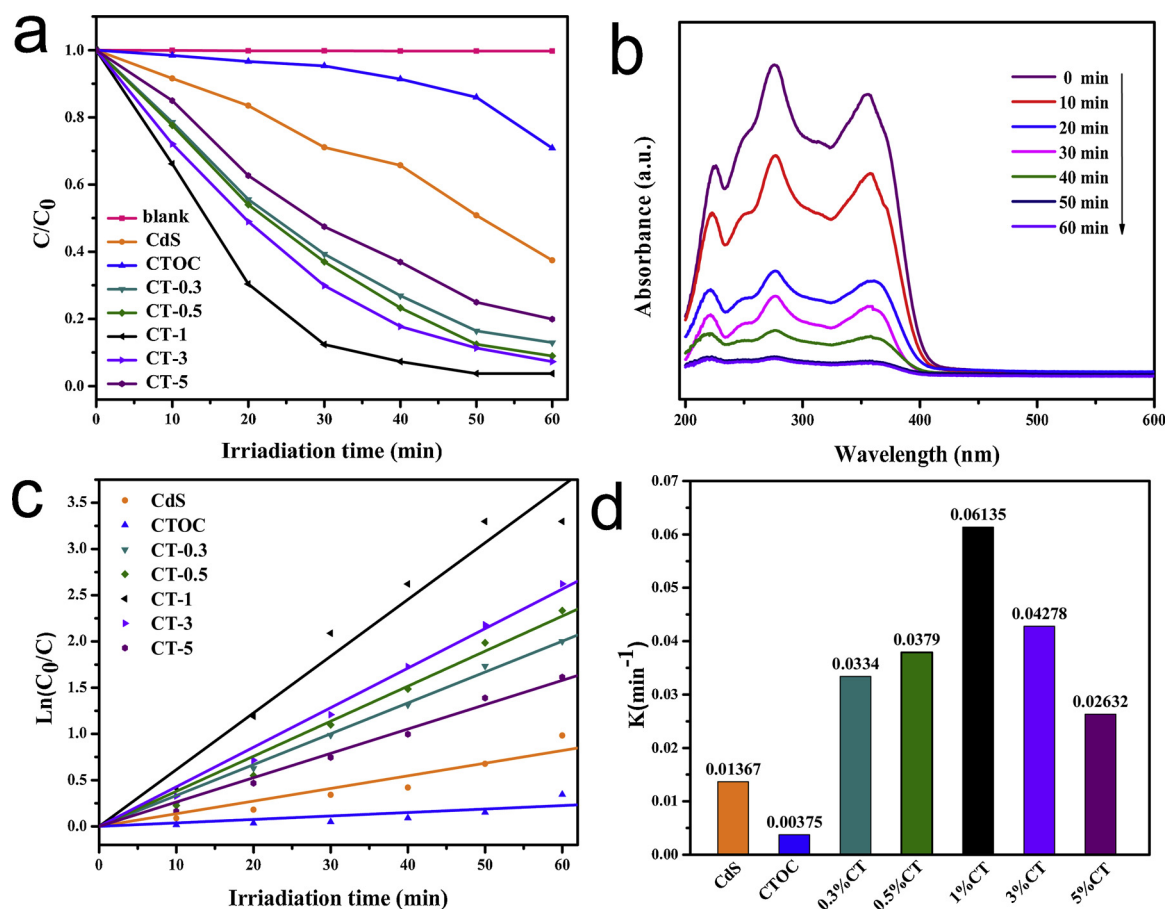**Fig. 5.** (a) Nitrogen sorption isotherm and (b) absorption properties of TC of all as-prepared samples.

Fig. 6. (a) Photocatalytic degradation of TC over as-prepared photocatalysts under visible irradiation ($\lambda > 420$ nm). (b) Changes in the characteristic absorption of TC at different irradiation times obtained using CT-1 as a photocatalyst. (c) The first-order kinetic plots and (d) apparent rate constants of the prepared samples for TC degradation.
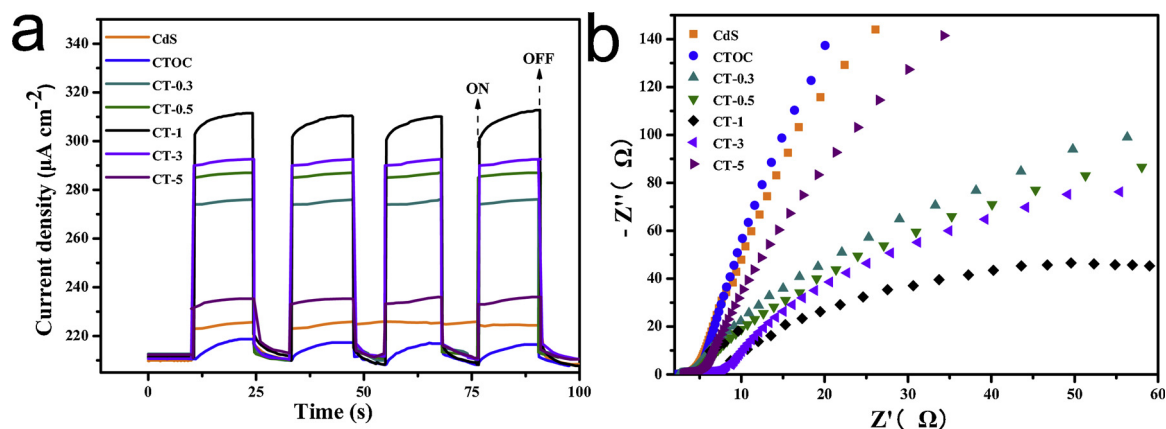

Fig. 7. (a) Transient photocurrent responses and (b) EIS changes of all as-prepared samples.

h^+ are the important active species in the photocatalytic reaction. Applying the IPA, the photocatalytic degradation rate only drops to 42%, which illustrates •OH is not the critical reaction species. Meanwhile, the ESR was also used to further determine the specific mechanism of the photocatalytic progress. From Fig. 8a-c, we can observe that the characteristic peaks of Ti^{3+} species ($g_x = 1.980$, $g_y = 1.953$, and $g_z = 1.889$) [55], DMPO-$\cdot O_2^-$ and DMPO-$\cdot OH$ are present in visible-light irradiation, in contrast to the peaks observed for CT-1 in the dark, effectively confirming the coexistence of Ti^{3+}, $\cdot O_2^-$ and $\cdot OH$ during the photocatalytic process. The stability of the photocatalyst is a very important factor in practical application. In order to estimate the

stability of the CdS/cluster composite, a cycling experiment for CT-1 photocatalytic degradation of TC was performed. As shown in Fig.S6, after five cycles of degradation, the photocatalytic performance of the CdS/CTOC composite photocatalyst had almost no decrease, indicating that the CdS/CTOC composite has good stability. The XRD pattern of the CdS/CTOC samples did not change significantly after five cycles (Fig.S7), which also proves that the long-term durability of the CdS/CTOC composites is satisfactory.

Based on the above analysis, we propose the photocatalytic mechanism over CdS/CTOC and present corresponding reaction model (Fig. 9). On the interface of CdS/CTOC, the electrons and holes of CdS
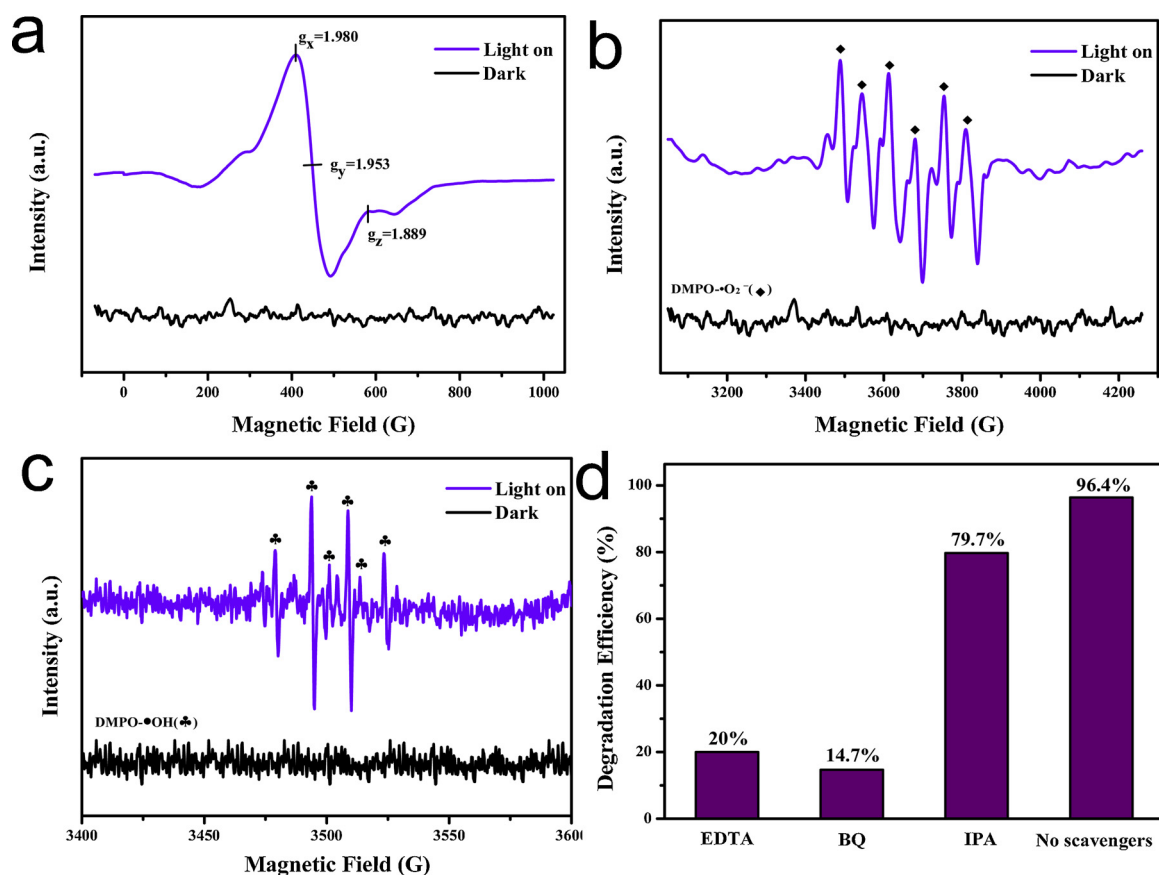
Fig. 8. (a–c) ESR spectra of CT-1 with or without visible-light irradiation (λ > 420 nm). (d) Trapping experiment of active species during the photocatalytic degradation of TC over CT-1 under visible light.
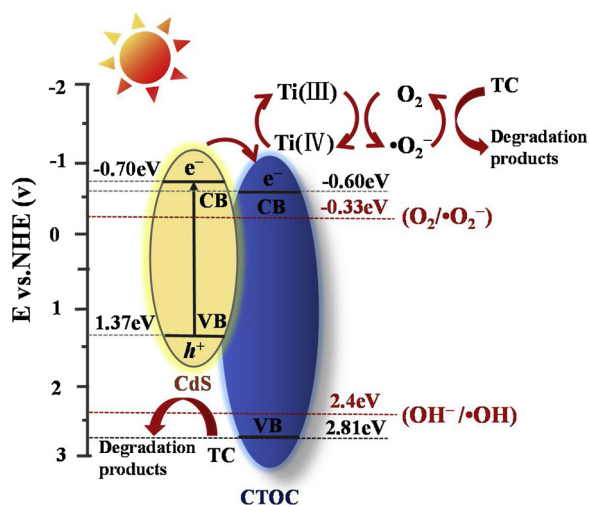

Fig. 9. Schematic diagram of the photoexcited electron-hole separation process on the interface of CdS/cluster composites under visible-light irradiation.

can first be separated under visible-light irradiation because of the narrow energy bandgap (Eg < 2.4), which the electrons are moved to the CB, departing from holes in the VB. Then, a great many electrons in CdS tend to migrate to the CB of CTOC, conducing to the formation of Ti^{3+} species in the active sites on the surface of the CdS/CTOC composites. Subsequently, the Ti^{3+} existed in CTOC is photo-oxidized into Ti^{4+} by combining with surface-absorbed oxygen to form superoxide radicals ($\cdot O_2^-$). Meanwhile, some $\cdot O_2^-$ can convert to less $\cdot OH$ to participate collectively in the photocatalytic process [56]. Simultaneously, the hole staying on the VB of CdS particles can rapidly oxidize

TC, resulting in more photogenerated charges (e^- and h^+) would have more opportunities for participating in degradation reaction. Based on the above analysis, photoexcitation charge carrier pairs can be efficiently divided by the surface active sites by the constitution of a composite structure between CdS and CTOC.

In order to investigate the photocatalytic degradation routes of TC over CdS/CTOC composites, LC−MS was used to analyze the TC solution with different illumination times. Fourteen intermediates were observed in the mass spectra (Fig.S8) and two degradation pathways are proposed (Fig. 10): First, a large amount of TC molecules ($m/z = 445$) were adsorbed on the surface of the CdS/CTOC composites due to its high specific surface area and abundant micropores. After reaching the adsorption equilibrium, the samples were exposed toward visible light to produce rich $\cdot O_2^-$, $\cdot OH$ and h^+ instantly. A part of TC molecules ($m/z = 445$) were attacked directly by light-induced h^+ and gradually demethylated to produce two intermediate products ($m/z = 431$ and $m/z = 417$) [57]. Another part of TC molecules ($m/z = 445$) underwent a hydroxylation reaction (addition reaction) under contact with $\cdot O_2^-$ and $\cdot OH$ to yield a new intermediate ($m/z = 461$) [58]. As the reaction continued, the other two intermediates ($m/z = 431$ and $m/z = 447$) were produced via detaching of functional groups [59]. Afterwards, the above macromolecular intermediates were gradually split into a plurality of small molecule intermediates ($m/z = 288, 279, 305, 220, 235, 211$) [60] under the assault of h^+, $\cdot O_2^-$ and $\cdot OH$. Eventually, the above organic intermediates will be mineralized to CO_2, H_2O and other inorganic substances under the action of active species to complete the degradation of TC.

4. Conclusion

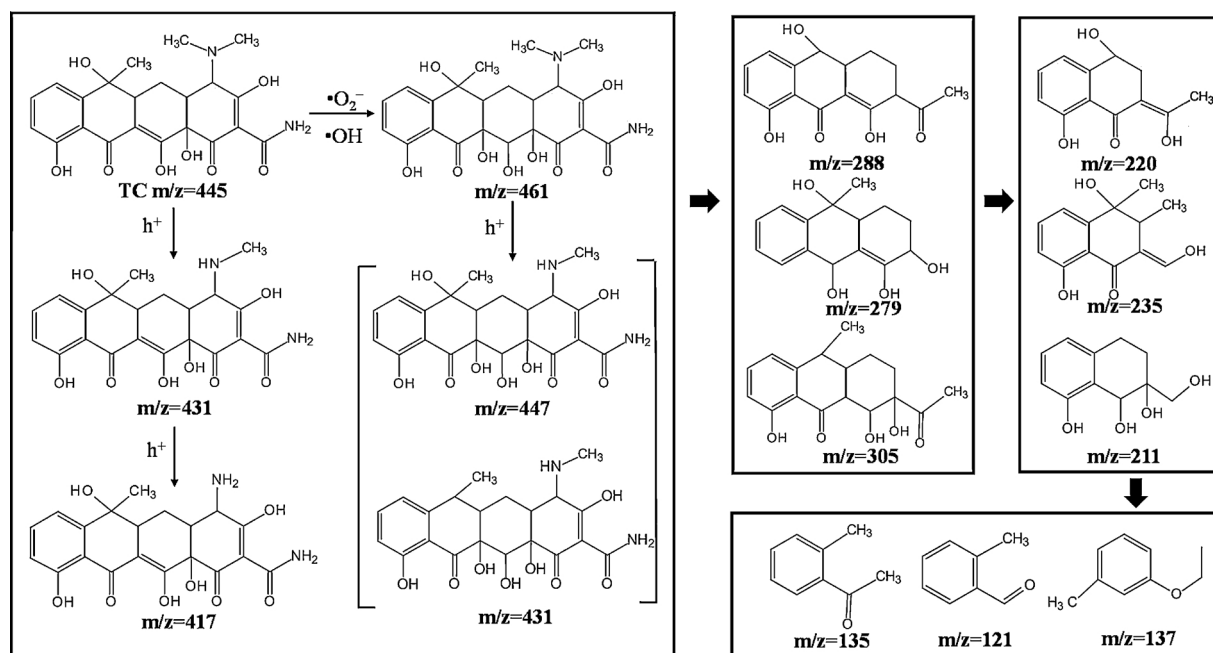In summary, a series of CdS/CTOC composite photocatalysts were

Fig. 10. Proposed intermediates and degradation routes of TC with light-induced h^+, $\cdot OH$ and $\cdot O_2^-$.

prepared through in situ precipitation and ultrasonic methods to degradation of TC under visible-light irradiation. The above experimental discussion indicates that all the CdS/CTOC composites exhibit remarkable enhanced photocatalytic performance and photostability compared to those of pristine CdS and CTOC. The reinforced photocatalytic ability can owe to the expanding response to the visible-light region, increased number of reactive sites and valid separation of photogenerated charge carrier pairs between the CdS active sites. Ti^{3+}, $\cdot O_2^-$ and h^+ play an important role during the degradation of TC with CdS/cluster composite photocatalysts. Intermediates over CdS/CTOC were determined and corresponding degradation mechanism of TC were discussed. This research could boost new insight on CdS/cluster binary composite systems to effectively degrade organic pollutants, which given a strategy for application on practical industry.

Acknowledgments

Appendix A. Supplementary data

Supplementary material related to this article can be found, in the online version, at doi:https://doi.org/10.1016/j.apcatb.2019.05.006.

References

[1] M. Conde-Cid, D. Fernandez-Calvino, J.C. Novoa-Munoz, M. Arias-Estevez, M. Diaz-Ravina, M.J. Fernandez-Sanjurjo, A. Nunez-Delgado, E. Alvarez-Rodriguez, Sci. Total Environ. 635 (2018) 1520–1529.
[2] S. Fu, K. Chen, H. Zou, J. Xu, Y. Zheng, Q. Wang, Energy Convers. Manage. 172 (2018) 588–594.
[3] X. Wang, D. Ryu, R.H. Houtkooper, J. Auwerx, Bioessays 37 (2015) 1045–1053.
[4] J.E. Moore, J.R. Rao, P.J.A. Moore, B.C. Millar, C.E. Goldsmith, A. Loughrey, P.J. Rooney, Aquat. Microb. Ecol. 44 (2010) 349–358.
[5] L. Zhou, Q.L. Wu, B. Zhang, Y. Zhao, B. Zhao, Environ. Sci.-Proc. Imp. 18 (2016) 500–513.
[6] Z. Li, Y. Sun, J. Xing, Y. Xing, A. Meng, J. Hazard. Mater. 352 (2018) 204–214.
[7] J. Cao, Z. Yang, W. Xiong, Y. Zhou, Y. Peng, X. Li, C. Zhou, R. Xu, Y. Zhang, Chem. Eng. J. 353 (2018) 126–137.
[8] T. Muhmood, M. Xia, W. Lei, F. Wang, M.A. Khan, Eur. J. Inorg. Chim. (2018) 1726–1732.
[9] X. Chu, G. Shan, C. Chang, Y. Fu, L. Yue, L. Zhu, Front. Environ. Sci. Eng. China 10 (2016) 211–218.
[10] J. Jiang, W. Shi, F. Guo, S. Yuan, Inorg. Chem. Front. 5 (2018) 1438–1444.
[11] W. Shi, F. Guo, M. Li, Appl. Surf. Sci. 473 (2019) 928–933.
[12] M. Wen, G. Li, H. Liu, J. Chen, T. An, H. Yamashita, Environ. Sci. Nano 6 (2019) 1006–1025.
[13] Z. Song, B. Hong, X. Zhu, F. Zhang, S. Li, J. Ding, X. Jiang, J. Bao, C. Gao, S. Sun, Appl. Catal. B: Environ. 238 (2018) 248–254.
[14] Z. Liu, G. Liu, X. Hong, Acta. Phys.-Chim. Sin. 35 (2019) 215–222.
[15] K. Wu, Acta. Phys.-Chim. Sin. 35 (2019) 135–136.
[16] K.L. Sowers, Z. Hou, J.J. Peterson, B. Swartz, S. Pal, O. Prezhdo, T.D. Krauss, Chem. Phys. 471 (2016) 24–31.
[17] Y. Yang, W. Zhang, Y. Xu, H. Sun, Appl. Surf. Sci. 452 (2018) 58–66.
[18] P. Gao, J. Liu, T. Zhang, D.D. Sun, W. Ng, J. Hazard. Mater. 229-230 (2012) 209–216.
[19] S. Velanganni, S. Pravinraj, P. Immanuel, R. Thiruneelakandan, Phys. B 534 (2018) 56–62.
[20] G.S. Li, D.Q. Zhang, J.C. Yu, Environ. Sci. Technol. 43 (2009) 7079–7085.
[21] T. Hirai, Y. Bando, J. Colloid Interface Sci. 288 (2005) 513–516.
[22] Y.R. Su, J. Choi, W. Balcerski, T. Kyu Lee, M.R. Hoffmann, Ind. Eng. Chem. Res. 46 (2007) 7476–7488.
[23] H. Chen, W. Li, H. Liu, L. Zhu, Electrochem. Commun. 13 (2011) 331–334.
[24] D. Xu, Y. Xu, D. Chen, G. Guo, L. Gui, Y. Tang, Chem. Phys. Lett. 325 (2000) 340–344.
[25] Y. Huang, J. Chen, W. Zou, Dalton Trans. 45 (2015) 1160–1165.
[26] A. Sinhamahapatra, H. Lee, S. Shen, S.S. Mao, J. Yu, Appl. Catal. B: Environ. 237 (2018) 613–621.
[27] C. Fleischer, A. Chatzitakis, T. Norby, Mater. Sci. Semicon. Proc. 88 (2018) 186–191.
[28] Z. Chen, P. Chen, P. Xing, X. Hu, H. Lin, Y. Wu, L. Zhao, Y. He, Fuel 233 (2018) 486–496.
[29] J. Roujean, J. Leon-Tavares, B. Smets, P. Claes, F. Camacho De Coca, J. Sanchez-Zapero, Remote Sens. Environ. 215 (2018) 57–73.
[30] J. Xu, Y. Li, X. Xu, J. Zhang, Y. Zhang, X. Yu, D. Huang, Ann. Nucl. Med. 32 (2018) 446–452.
[31] S. Contreras, J.P. Werne, A. Araneda, R. Urrutia, C.A. Conejero, Sci. Total Environ. 630 (2018) 878–888.
[32] J. Chen, X. Pang, H. Pang, Energy Explor. Exploit. 36 (2018) 1335–1355.
[33] X. Li, H. Liu, X. Jia, G. Li, T. An, Y. Gao, Sci. Total Environ. 621 (2018) 1533–1541.
[34] C. Zhao, Y. Han, S. Dai, X. Chen, J. Yan, W. Zhang, H. Su, S. Lin, Z. Tang, B.K. Teo, N. Zheng, Angew. Chem. Int. Ed. Engl. 56 (2017) 16252–16256.
[35] C.H.L. Kennard, G. Smith, E.J. O'Reilly, Inorg. Chim. Acta Rev. 59 (1982) 241–247.
[36] J. Shi, X. Yan, H. Cui, X. Zong, M. Fu, S. Chen, L. Wang, J. Mol. Catal. A-Chem. 356 (2012) 53–60.
[37] F. Guo, W. Shi, X. Lin, X. Yan, Y. Guo, G. Che, Sep. Purif. Technol. 141 (2015) 246–255.
[38] L. Ge, F. Zuo, J. Liu, Q. Ma, C. Wang, D. Sun, L. Bartels, P. Feng, J. Phys. Chem. C 116 (2012) 13708–13714.

[39] J. Lee, Thin Solid Films 451 (2004) 170–174.
[40] L. Óvári, S.K. Calderon, Y. Lykhach, J. Libuda, A.E. Helyi, J. Catal. 307 (2013) 132–139.
[41] G. Yang, Z. Jiang, H. Shi, T. Xiao, Z. Yan, J. Mater. Chem. 20 (2010) 5301–5309.
[42] G. Yang, Z. Yan, T. Xiao, Appl. Surf. Sci. 258 (2012) 8704–8712.
[43] L. Qi, J. Yu, M. Jaroniec, Phys. Chem. Chem. Phys. 13 (2011) 8915–8923.
[44] X. Fang, Y. Yuan, H. Han, D. Wu, Z. Gao, Cryst. Eng. Comm. 14 (2012) 3615–3622.
[45] W. Shi, F. Guo, S. Yuan, Appl. Catal. B: Environ. 209 (2017) 720–728.
[46] W. Yang, L. Zhang, J. Xie, X. Zhang, Q. Liu, Angew. Chem. Int. Ed. 55 (2016) 6716–6720.
[47] H.G. Kim, P.H. Borse, W. Choi, J.S. Lee, Angew. Chem. Int. Ed. 117 (2010) 4661–4665.
[48] G. Liu, P. Niu, L. Yin, H. Cheng, J. Am. Chem. Soc. 134 (2012) 9070–9073.
[49] W. Shu, Z. Lei, L. Bai, J. Yan, Q. Jiang, J. Mater. Chem. A Mater. Energy Sustain. 2 (2014) 7439–7445.
[50] B.A. Pinaud, Z. Chen, D.N. Abram, T.F. Jaramillo, J. Phys. Chem. C 115 (2011) 11830–11838.
[51] Y. Chen, D.D. Dionysiou, J. Mol. Catal. A Chem. 244 (2006) 73–82.
[52] C. Zhao, M. Pelaez, X. Duan, H. Deng, K. O'Shea, D. Fatta-Kassinos, D.D. Dionysiou, Appl. Catal. B: Environ. 134-135 (2013) 83–92.
[53] L.B. Khalil, W.E. Mourad, M.W. Rophael, Appl. Catal. B: Environ. 17 (1988) 267–273.
[54] W. Shi, F. Guo, M. Li, J. Alloys. Compd. 775 (2019) 511–517.
[55] Y. Wu, W. Luo, Y. Wang, Y. Pu, X. Zhang, L. You, Q. Zhu, J. Dai, Inorg. Chem. 51 (2012) 8982–8988.
[56] F. Dong, Z. Wang, Y. Li, Environ. Sci. Technol. 48 (2014) 10345–10353.
[57] S. Jiao, S. Zheng, D. Yin, Chemosphere 73 (2008) 377–382.
[58] Y. Wang, H. Zhang, J. Zhang, J. Hazard. Mater. 192 (2011) 35–43.
[59] A. Di Paola, M. Addamo, V. Augugliaro, E. Garcia-Lopez V, Fresenius Environ. Bull. 13 (2004) 1275–1280.
[60] I. Dalmázio, M.O. Almeida, R. Augusti, T.M.A. Alves, J. Am. Soc. Mass Spectrom. 18 (2007) 679–687.